Supplementary Information

The molecular architecture of the desmosomal outer dense plaque by integrative structural modeling

Satwik Pasani[1], Kavya S Menon[1], Shruthi Viswanath[1, *]

[1] National Center for Biological Sciences, Tata Institute of Fundamental Research, Bengaluru 560065, India

* Corresponding Author: shruthiv@ncbs.res.in (SV)

Section 1: Modeling

Section: 1.1 Stoichiometry Simulations

The number of molecules that could be accommodated in the PG layer was unclear since it was not possible to unambiguously dock the molecules manually in this region. A higher number would result in an overcrowded model or push molecules outside the envelope of the cryo-ET density map, while a smaller number would not be enough to explain the whole density map. To determine this, we performed separate simulations ("stoichiometry simulations") that only included the PG and DP molecules and the PG layer EM density. We ran six simulations, each with an equal number of PG and DP molecules ranging from 2 to 7. Each stoichiometry simulation consisted of five independent runs. For each of these runs, the representation and sampling followed the IMP modeling protocol (Saltzberg et al., 2021; Viswanath et al., 2017). The restraints applied included the EM restraint, the immuno-EM restraint, the excluded volume restraint, the connectivity restraint, and the cylinder restraint to ensure that the molecules are not too far away from the cryo-ET map. 3 million models were simulated per stoichiometry. After filtering the models sampled before equilibration, the top 10% of models were determined based on the cross-correlation coefficient of the models to the cryo-ET map (Bonomi et al., 2019) (Fig. S1). In summary, an ensemble of models was computed for each stoichiometry to estimate the uncertainty around stoichiometry and determine which stoichiometry best fits the cryo-ET map. The uncertainty in stoichiometry is captured by error bars representing the standard deviation of the cross-correlation values (Fig. S1). The error bars are overlapping for 3,4, and 5 molecules of PG/DP, which suggests that these stoichiometries do not have a large significant difference between them in their fit to the map (Fig. S1).

Based on the above results and the following considerations, the number of PG/DP molecules was taken to be four. The average cross-correlation for four molecules was only slightly lower than the cross-correlation for three PG/DP molecules. Further, selecting four PG/DP copies allowed selecting of four PKPs in the PKP layer including the central PKP without introducing any asymmetries in the selection. It also allowed us to maintain 1:1:1:1 stoichiometry for PG:DP:PKP:DC with equal numbers of DSC and DSG (2 each). Finally, it was consistent with previous studies which showed that no more than four PG and DP molecules each could fit in the PG layer (Al-Amoudi et al., 2011).

Section: 1.2 Restraints

Distance threshold for sequence connectivity restraint

To set up the connectivity restraint, we need to scale the inter-bead distance to allow the more disordered N/C termini as well as the DC proteins to span a greater end-to-end distance compared to the globular protein domains. For each protein domain with at least a partial disorder (for example, PKP-N, DP-N, etc), we first find the radius of gyration of this fragment assuming the fragment to be completely disordered, using $R_g = 1.92N^{0.6}$(Kohn et al., 2004) where *N* is the number of residues. We model the fragment as a chain of monomers composed of *n* statistically independent segments each of length *a*. We assume *n* to be approximately equal to the number of beads in our representation of the fragment as two adjacent beads are free to be in any relative orientation without any other restraints; *a* is then the inter-bead distance. We then use a relation between the RMS Distance between the two ends of the chain ($R_F = an^{0.6}$) and the radius of gyration (R_G) to estimate *a* for our fragment: ${R_G}^2/{R_F}^2 = 25/176$ (Teraoka, 2002). Another estimate for *a* is calculated internally in IMP and comes from the assumption that the fragment is globular (Alber et al., 2007). The final scaling depends on the weighted sum of these

two estimates, the weights corresponding to the portion of the fragment predicted to be disordered by PSIPRED (Buchan & Jones, 2019). Given an estimate of *a*, we can calculate the surface-to-surface distance for adjacent beads to create an harmonic upper bound restraint such that the beads are only penalized when they are farther than this distance apart. We use the maximum end-to-end distance (*an*) and find the bead surface-to-surface distance needed to achieve this end-to-end distance. This is approximated by the following relation where *r* is the typical radius of a bead in our model: $d = (an - 2r)/n - 2r$. The calculated scale matches the scale calculated using a more accurate measure for ${R_G}^2/{R_F}^2 \approx 0.95/6$ given by renormalization theory (Teraoka, 2002) up to rounding. However, the scale is only a heuristic parameter and the results obtained are relatively robust to its exact value.

Section 2: Analysis

Section: 2.1 Filtering based on Autocorrelation

To filter a computationally feasible subset of models from the large set of sampled models, we first remove the initial few models based on statistical testing (Chodera, 2016; Saltzberg et al., 2021), to consider only the models after equilibration assumed to be in the stationary distribution. Next, we only take every 20th model in the MCMC sampling run (PMI analysis parameter nskip=2, writing every 10th frame to disk). To identify an appropriate number of models to skip, we ran eight independent single replica runs with all the restraints. We analyzed the spatial autocorrelation of the XYZ coordinates of each bead along the sampling trajectory. We chose as our cutoff the smallest number of sampling steps after which the autocorrelation of all the beads had fallen to at most 85-90%. This allows us to remove the highly correlated models to obtain an independent set of models to analyze downstream.

Section: 2.2 Cross-Correlation of Localization Densities and cryo-ET maps

We first computed the predicted localization density by combining the densities from all modeled proteins for the major cluster separately for the PKP layer (PKP-S) and PG-Layer (PG-N,S,C, DP-N,S). We then calculated the cross-correlation between the predicted density and the reference cryo-electron tomography map by calculating the Pearson correlation between the voxel-wise values in the two maps. This is calculated at all grid points at a voxel spacing of 5Å spread over the volume enclosing both the predicted localization density and the cryo-ET map. The values of the maps at these grid points were found by interpolation (RegularGridInterpolator in scipy (Virtanen et al., 2020)). This is similar to calculating Correlation around the mean in UCSF Chimera (fitmap) except that the Chimera calculation only involves the non-zero grid points of the reference map, causing the correlation value to change depending on the order of the two maps.

Supplementary Figures

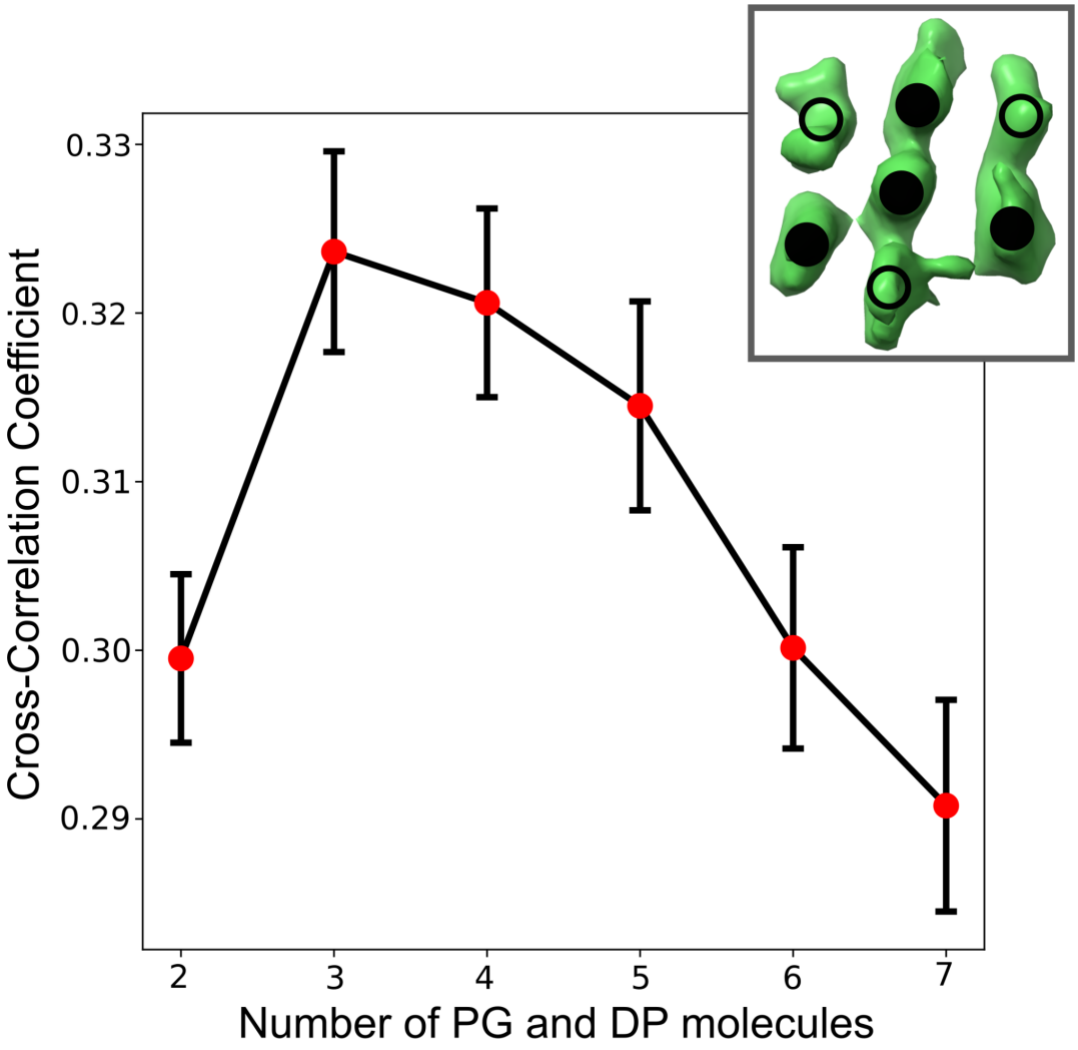

Figure S1 Estimating the number of PG and DP molecules and selecting the layout for PKP1 molecules. The graph shows the results for stoichiometry simulations with the number of PG and DP molecules ranging from 2 to 7. The boxplot marks the mean (red dot) and the standard deviation (black error bars) of the cross-correlation coefficient (Bonomi et al., 2019) between the top 10% of models with the best cross-correlation scores and the cryo-ET map. **(Inset)** The seven densities in the PKP layer of the cryo-ET map (top view) are shown. Of these, four were full-length PKPs in our model (filled circles) and three were fixed, non-interacting PKP1-S regions (empty circles). See also Methods, Stage 2, and Supplementary Section 1.1.

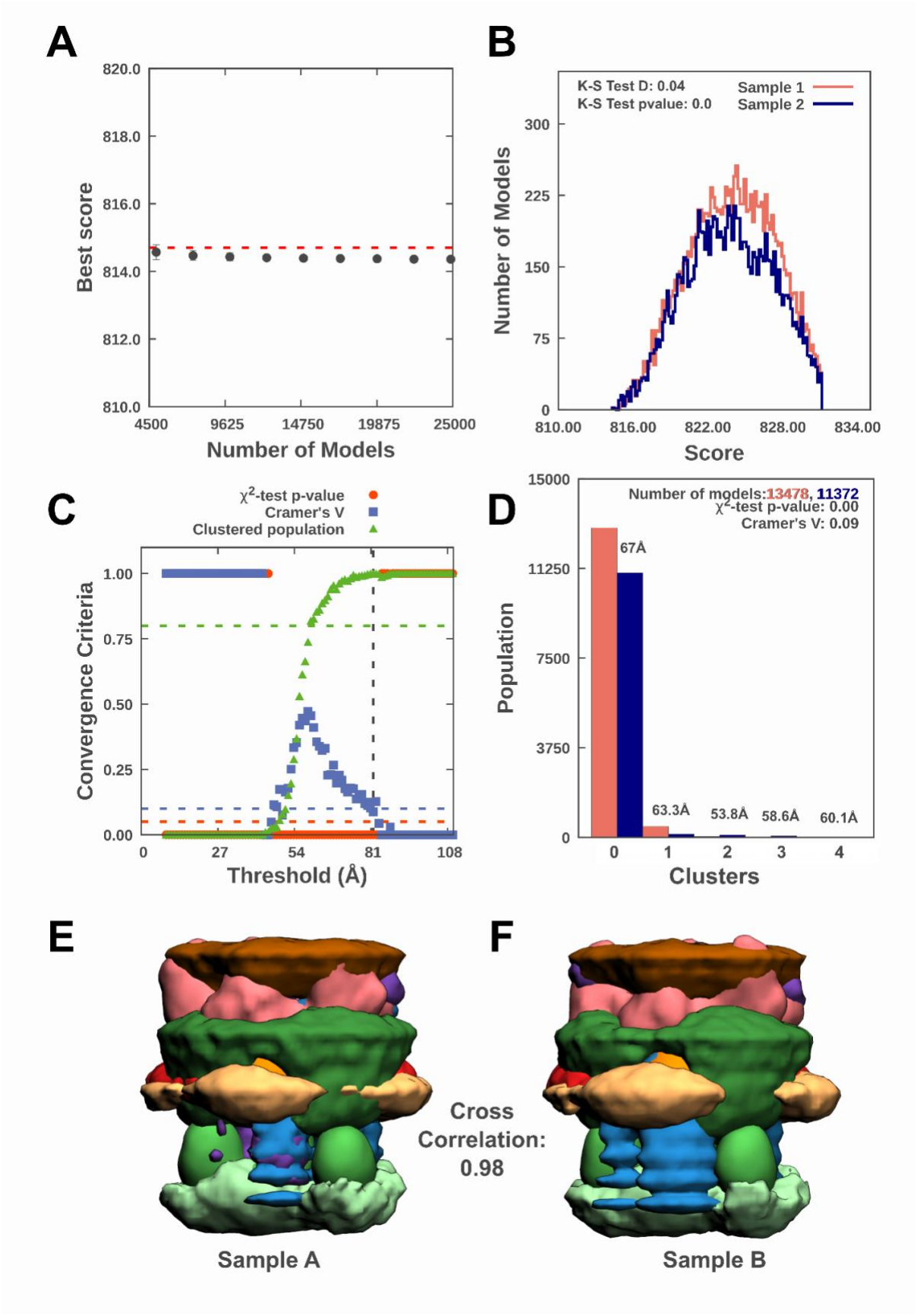

Figure S2 Sampling Exhaustiveness protocol for Desmosomal ODP A) Test for the convergence of the model score for the 24016 good-scoring models. The scores do not continue to improve as more

models are added independently. The error bar represents the standard deviations of the best scores, estimated by repeating sampling of models 10 times. The red dotted line indicates a lower bound reference on the total score. **B)** Testing the similarity of model score distributions between samples 1 (red) and 2 (blue). The difference in the distribution of scores is significant (Kolmogorov-Smirnov two-sample test p-value less than 0.05) but the magnitude of the difference is small (the Kolmogorov-Smirnov two-sample test statistic D is 0.04); thus, the two score distributions are effectively equal. **C)** Three criteria for determining the sampling precision (Y-axis), evaluated as a function of the RMSD clustering threshold (X-axis). First, the p-value is computed using the χ^2-test for homogeneity of proportions (red dots). Second, an effect size for the χ^2-test is quantified by the Cramer's V value (blue squares). Third, the population of models in sufficiently large clusters (containing at least 10 models from each sample) is shown as green triangles. The vertical dotted grey line indicates the RMSD clustering threshold at which three conditions are satisfied (p-value > 0.05 [dotted red line], Cramer's V < 0.10 [dotted blue line], and the population of clustered models > 0.80 [dotted green line]), thus defining the sampling precision of 82 Å. **D)** Populations of sample 1 and 2 models in the clusters obtained by threshold-based clustering using the RMSD threshold of 82 Å. Cluster precision is shown for each cluster **E-F)** Comparison of localization probability densities of models from sample A and sample B for the major cluster. The cross-correlation of the density maps (see Supplementary section 2.2) of the two samples is greater than 0.98 (Viswanath et al., 2017).

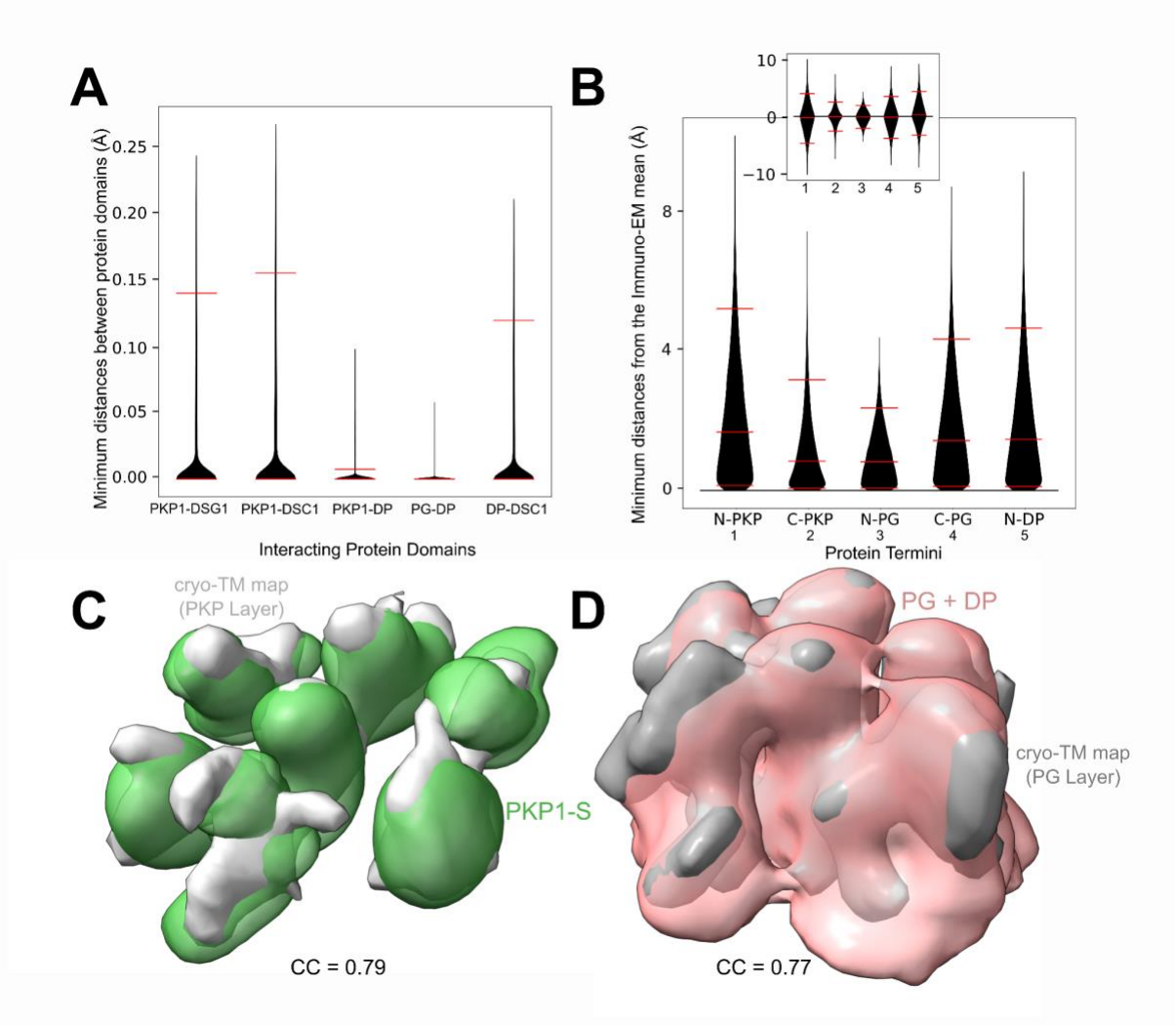

Figure S3 Fit to data used in modeling A) Fit to the data from biochemical experiments formulated as binding restraints (Methods). Each violin corresponds to the absolute closest distance between the two interacting domains across all protein copies for a model in the major cluster (Methods). Each distribution corresponds to a restraint in Table S2A. Red horizontal lines correspond to the 5th, 50th, and 95th percentile (in **A** and **B**) after outlier removal. **B)** Fit to immuno-EM data (North et al., 1999). Each violin corresponds to the absolute difference between the experimental mean and the model-predicted distance from the membrane across all protein copies for a model in the major cluster (Methods). The inset shows the same information without the absolute value (i.e. signed difference). **C-D)** Fit to the cryo-ET map for the PKP Layer (**C**) and the PG Layer (**D**). Densities from the model (colored) are shown along with the segmented densities from the cryo-ET map, EMD-1703 (Al-Amoudi et al., 2011) (Methods). The cross-correlation (CC) is mentioned for each of the fits (Methods, Supplementary Section 2.2). PKP1-S density (including the non-interacting PKP1 molecules) and the PG + DP density are visualized at a ~10% threshold and the map is visualized at the recommended threshold. See also Fig. 3, Table S2.

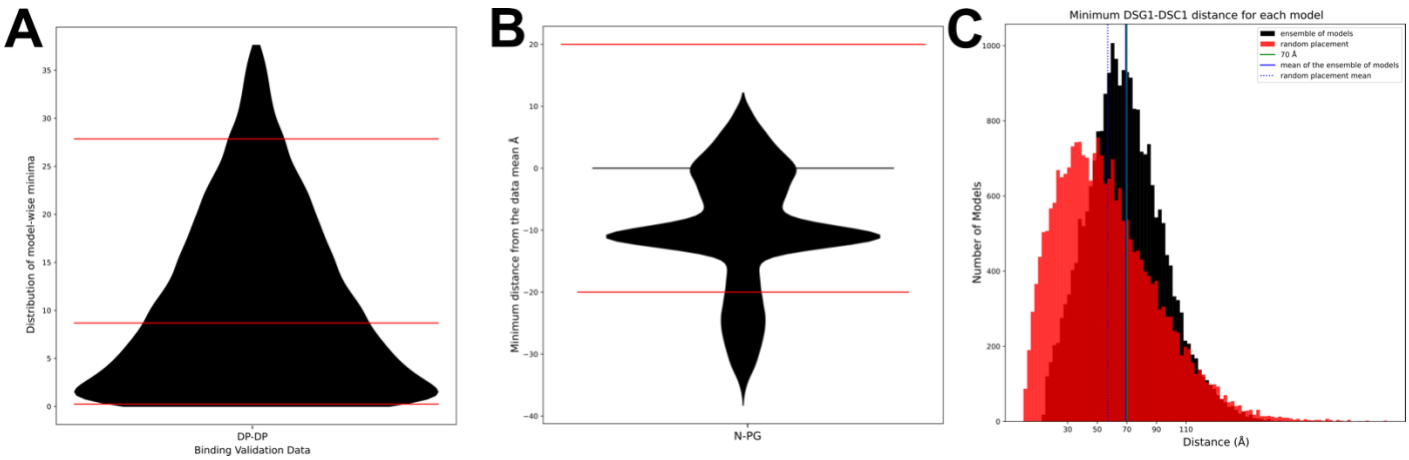

Figure S4 Fit to data not used in modeling A) Fit to the data from biochemical experiments not used for modeling (Methods). The violin corresponds to the closest distance between the two interacting domains across all copies for a model in the major cluster (Methods). Red horizontal lines correspond to the 5th, 50th, and 95th percentile after outlier removal. **B)** Fit to the super-resolution imaging data from (Stahley et al., 2016). The violin corresponds to the signed difference between the experiment mean and the model-predicted distance from the membrane across all protein copies for a model in the major cluster (Methods). The red lines show the standard deviation of the imaging data. **C)** Fit to the cadherin spacing data from (Sikora et al., 2020). The black histogram displays the minimum distance between DSC1-DSG1 at the plasma membrane for each model. The red histogram displays the corresponding distance in a null model, where the membrane-anchored DSG1 and DSC1 beads are placed at random within a circle defined by the extent of the cryo-ET map. The data from (Sikora et al., 2020) (green line), the mean of the distribution from integrative models (blue solid line), and the mean of the distribution from the null model (blue broken line) are also depicted.

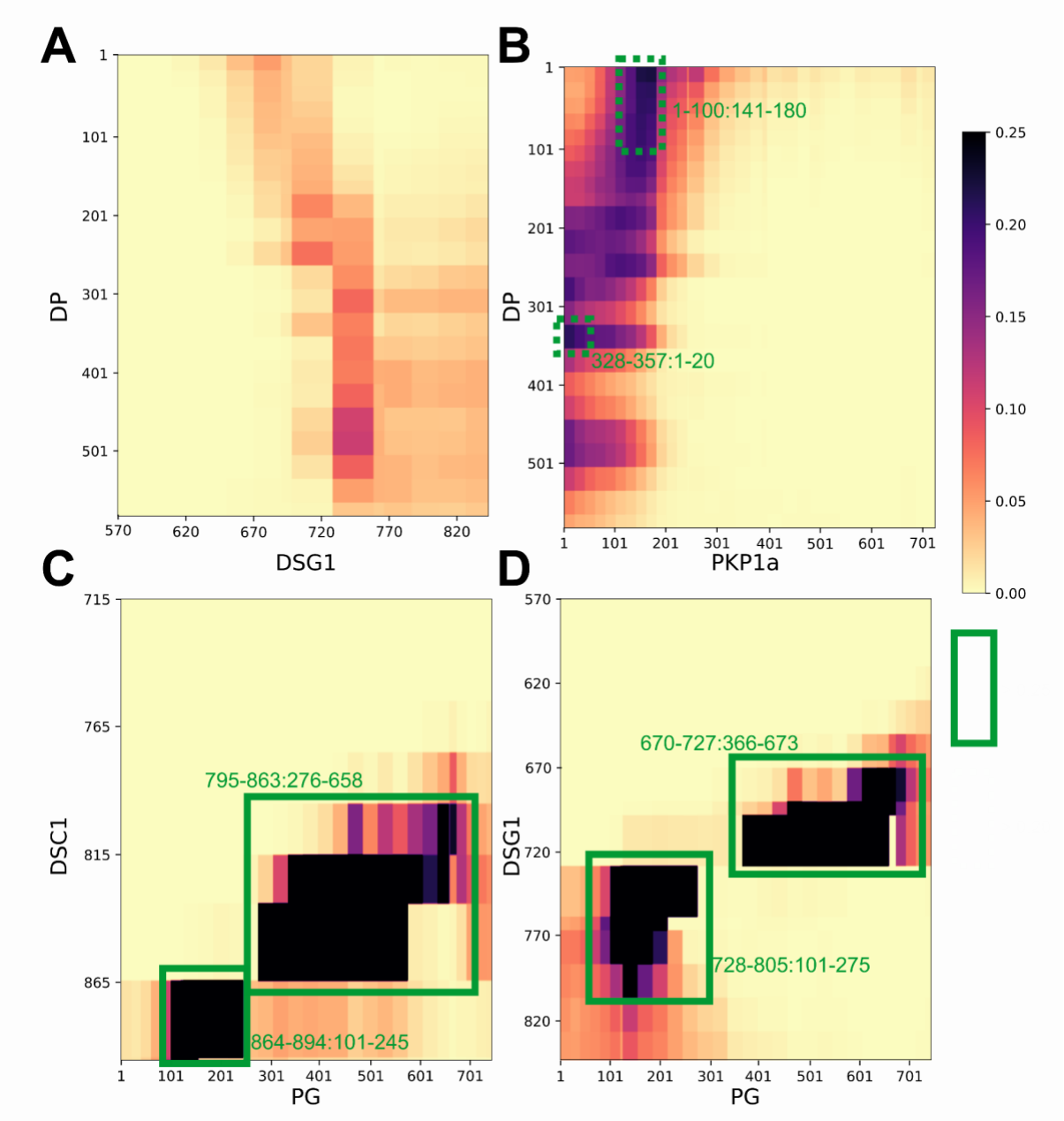

Figure S5 Additional contact maps Protein-protein contact maps for DP-DSG1 (**A**), DP-PKP1 (**B**), PG-DSC1 (**C**), and PG-DSG1 (**D**) pairs. Maps are colored by the proportion of the models in the major cluster where the corresponding two bead surfaces are within contact distance (10 Å). Rectangles with solid green (broken green) lines outline novel contacts present in >25% (>20%) of the models. Interacting residues are marked in green text in the format Y-axis protein residues: X-axis protein residues. See also Fig. 4 and Table S4.

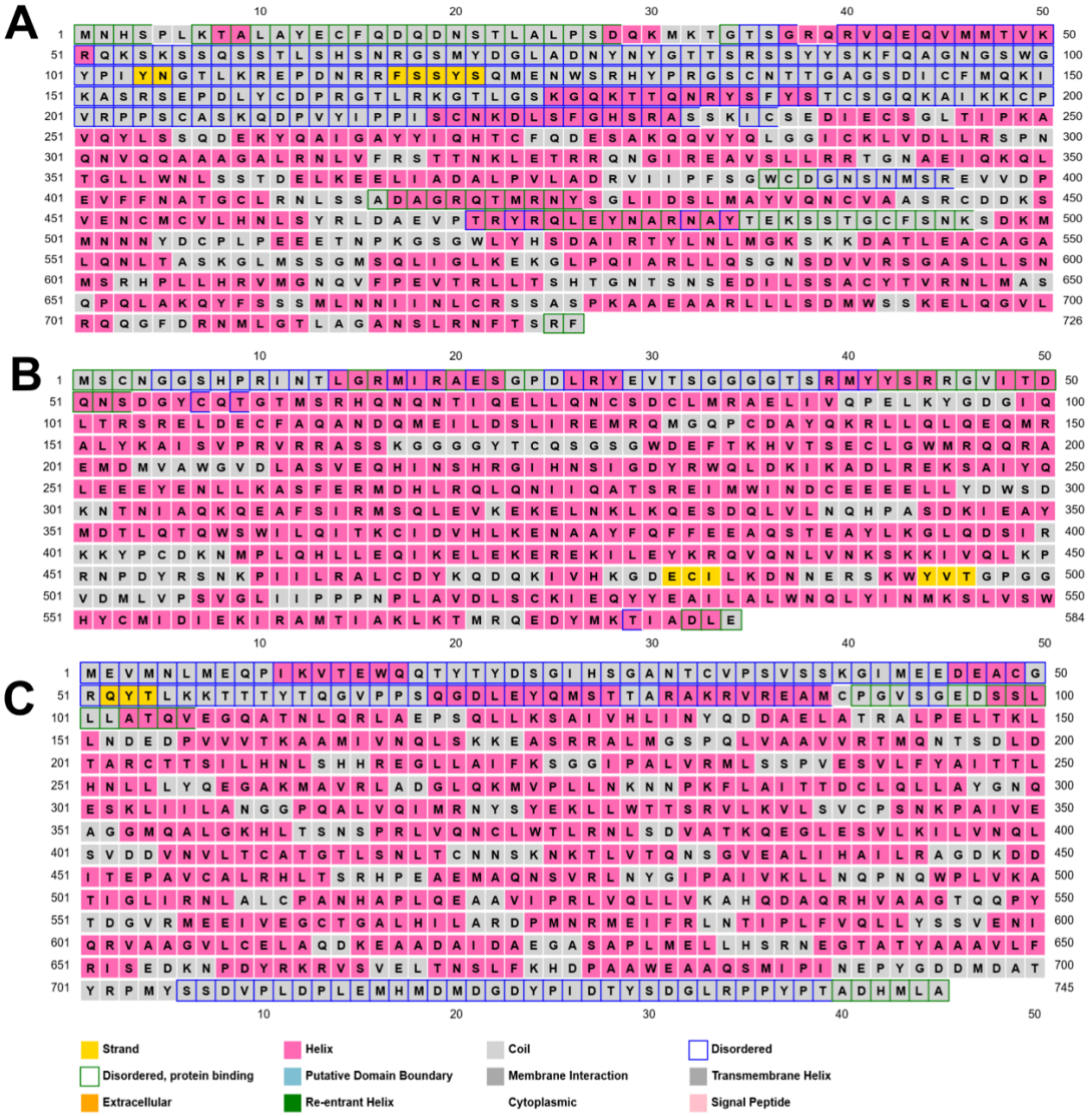

D

```
PKP1_CHICK      ------------------------------------------------MVCCFPLLL   9
PKP1_HUMAN      MNHSPLKTALAYECFQDQDNSTLALPSDQKMKTGTSGRQRVQEQVMMTVKRQKSKSSQSS   60
PKP1_MOUSE      MNHSPLKTALAYECFQDQDNSTLALPSDQKMKTGTSGRQRVQEQVMMTVKRQKSKSSQSS   60
                                                                  .

PKP1_CHICK      TVLFSFTGSMYDCVADGYG-YG-TSRGSYYTKTQMGNSSWGYPLYNGTLKRDAENRRYSS   67
PKP1_HUMAN      TLSHSNRGSMYDGLADNY-NYGTTSRSSYYSKFQAGNGSWGYPIYNGTLKREPDNRRFSS   119
PKP1_MOUSE      TLSHSNRGSMYDGLADNYNNYGTTSRSSYFSKFQAGNGSWGYPIYNGTLKREPDNRRFSS   120
                *: .*  ***** :**.*  ** ***.**::* * **.*****:*******: :***:**

PKP1_CHICK      YSQMEGWGSKHYSKAVCSPNRAGSDYCFVQNIKSSRSEPDLYCEPPRGTLRKSQVGGRAE   127
PKP1_HUMAN      YSQMENWS-RHYPRGSCNTTGAGSDICFMQKIKASRSEPDLYCDP-RGTLRKGTLGSK-G   176
PKP1_MOUSE      YSQMENWS-RHYPRGSCATPGAGSDICFMQKIKASRSEPDLYCDP-RGTLRKGTLGSK-G   177
                *****.*. :** :. *    **** **:*:**:********** :* ******. :*.:

PKP1_CHICK      HKATLNRQSIYSSCSTQQGTTRTSKKIPARALSCPSSNKPDVVYAQPVMSCKQDAVYGQA   187
PKP1_HUMAN      QKTTQNRYSFYSTCSGQKAI----KKCPVRPPSCASKQDP--VY-IPPISCNKDLSFGHS   229
PKP1_MOUSE      HKTTQNRCSFYSTCSGQKAV----KKCPVRPPSCTSKQDP--VY-VPPISCNKDLSFGHS   230
                :*:* ** *:**:** *:.     ** *.*  ** *.:.*  **  * :**::*  :*::
```

Figure S6 Prediction of disorder in PKP1, DP, and PG and sequence conservation for PKP1 The PSIPRED (Buchan & Jones, 2019) outputs for PKP1 (**A**), DP-N (**B**), and PG (**C**) are shown with the color scheme displayed below panel C. **D)** Sequence conservation output using Clustal Omega for Chick, Human and Mouse PKP1$^{1\text{-}229}$ (Goujon et al., 2010; Sievers et al., 2011). The colors represent different kinds of amino acids (acidic: blue, basic: magenta, hydrophobic/small: red, Hydroxyl/sulfhydryl/amine/G: green). An asterisk (*) represents an exact residue match, a colon (:) represents a strongly similar match, and a period (.) represents a weakly similar match.

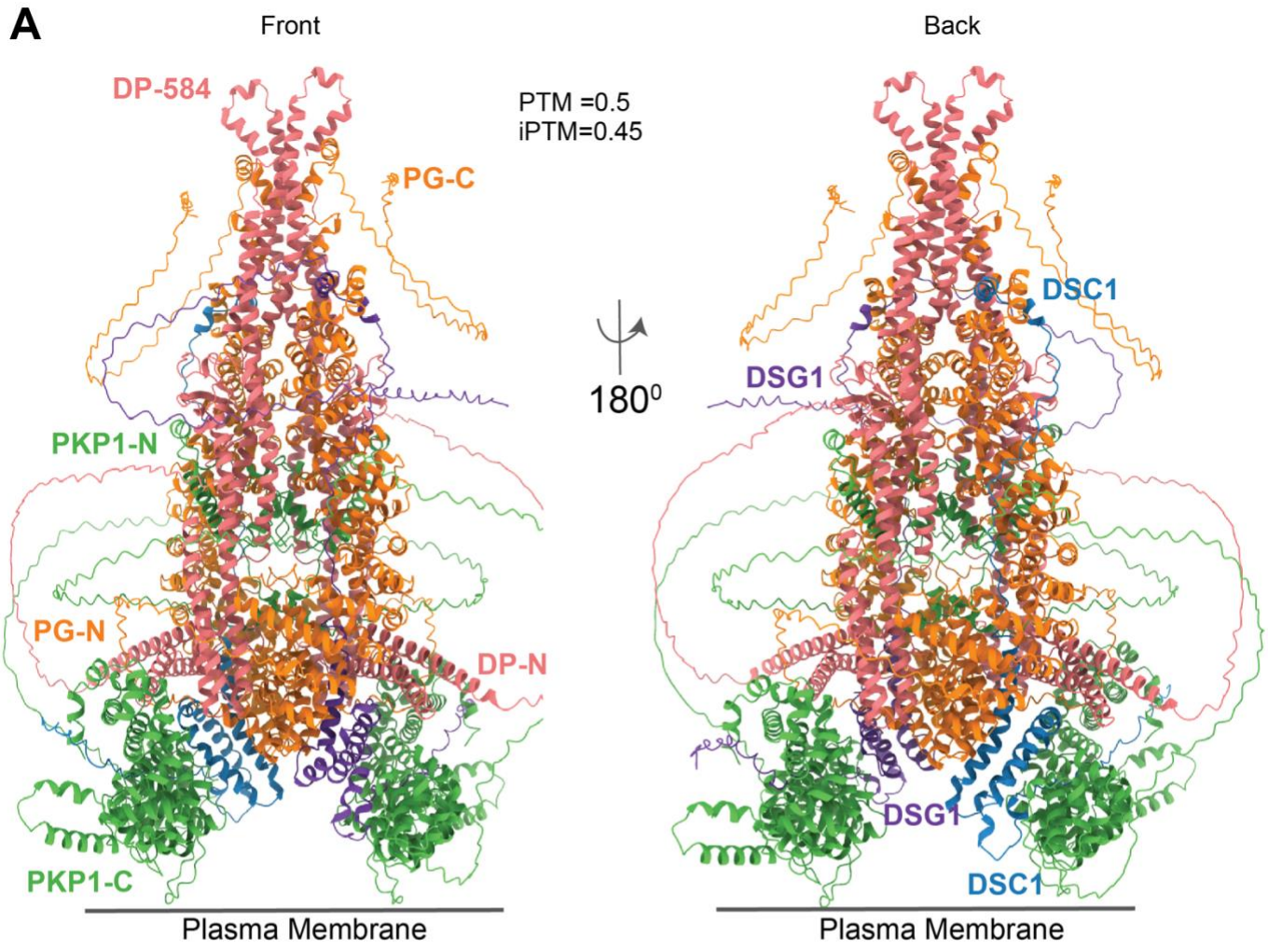
A
Front
Back
DP-584
PG-C
PTM =0.5
iPTM=0.45
180⁰
DSC1
DSG1
PKP1-N
PG-N
DP-N
DSG1
DSC1
PKP1-C
Plasma Membrane
Plasma Membrane

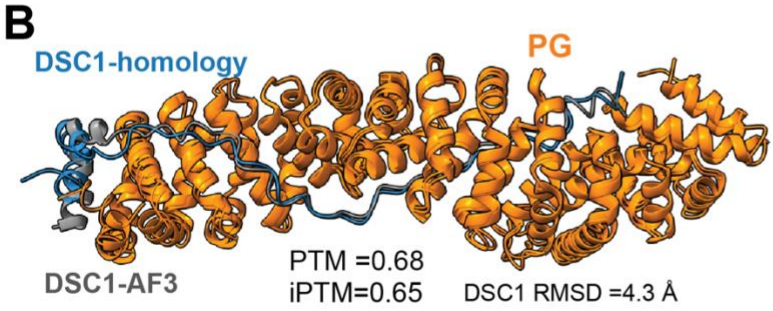
B
DSC1-homology
PG
DSC1-AF3
PTM =0.68
iPTM=0.65
DSC1 RMSD =4.3 Å

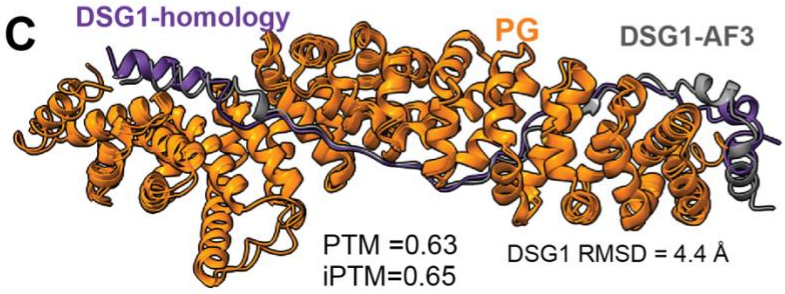
C
DSG1-homology
PG
DSG1-AF3
PTM =0.63
iPTM=0.65
DSG1 RMSD = 4.4 Å

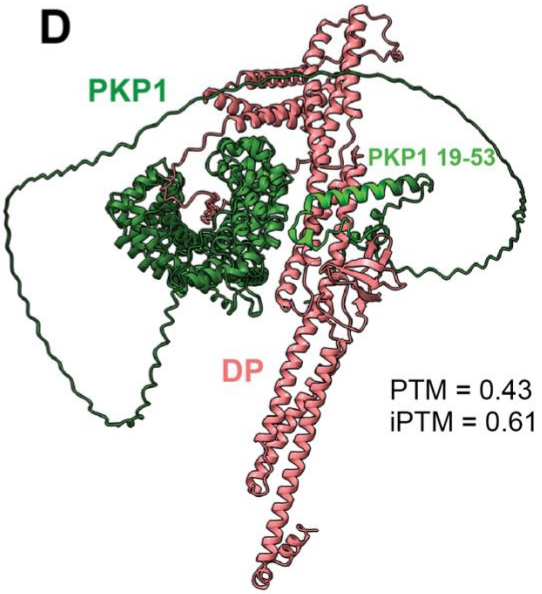
D
PKP1
PKP1 19-53
DP
PTM = 0.43
iPTM = 0.61

Figure S7 Alphafold3 predictions The best-ranked models, along with the corresponding PTM + IPTM scores from AF3 are displayed for **A)** the full desmosome ODP, **B)** PG-DSC1, **C)** PG-DSG1, and **D)** DP-PKP1. Only sequence regions corresponding to the ODP were submitted to Alphafold3 (e.g., DP-584 in **A** refers to the C-terminal end of DP in the ODP). Proteins are colored as in the main figures. **B)** and **C)**: only the residues from the AF3 model corresponding to the homology model are shown. The ligand RMSD between the AF3 model and the corresponding homology model is computed by superposing on PG (orange) and computing the RMSDs on DSC1 (blue: homology, grey:AF3) /DSG1(purple: homology, grey:AF3). **D)** The PKP1 residues at the interface to DP are shown (lime green).

Supplementary Tables

Protein	Domain name (abbreviation)	Residue Ranges	Structure: PDB (chain: residues) or unknown	Uniprot ID
DP1	N-terminal domain (DP-N)	1-177	Unknown	P15924-1
	Spectrin homology domain/plakin domain (DP-S)	178-584	3R6N (A: 178-584)	
PKP1a	N-terminal domain (PKP1-N)	1-243	Unknown	Q13835-2
	Armadillo-repeat domain (PKP1-S)	244-700	1XM9 (A: 244-700)	
	C-terminal domain (PKP1-C)	701-726	Unknown	
PG	N-terminal domain (PG-N)	1-125	Unknown	P14923
	Armadillo-repeat domain (PG-S)	126-673	3IFQ (A: 126-673)	
	C-terminal domain (PG-C)	674-745	Unknown	
DSG1a	DSG1a cytoplasmic ODP domain (DSG1a)	570-697	Unknown	Q02413-1
		698-765	3IFQ (C: 628-721)	
		766-842	Unknown	
DSC1a	DSC1a cytoplasmic domain (DSC1a)	715-833	Unknown	Q08554-1
		834-894	3IFQ (C: 628-721)	

Table S1 Modeled protein domains The different domains of the modeled proteins are shown along with their residue ranges. Regions of unknown structure were represented as flexible 20-residue beads, while regions of known structure were represented as rigid bodies consisting of 30-residue beads. The colors refer to domains without a known structure (red), domains which are homology modeled on a structure template of an isoform or homolog (yellow), and domains for which a structure exists in the PDB (green). Only the domains in the ODP were modeled; extracellular and transmembrane domains ($DSG1^{1-569}$, $DSC1^{1-714}$) and intracellular domains outside the ODP ($DP^{585-2871}$, $DSG1^{843-1049}$) were not modeled (Al-Amoudi et al., 2011; Garrod & Chidgey, 2008; Nilles et al., 1991).

Protein 1	Protein 2	Domain 1	Domain 2	Experiment	Reference	Data for Restraint Protein 1 residues: Protein 2 residues
PKP1a	DSG1	70-213	570-1049	Y2H	(Hatzfeld et al., 2000)	70-213:570-842
		1-286	568-1049	Y2H	(Kowalczyk et al., 1999)	
		1-726	499-1049	OA	(Smith & Fuchs, 1998)	
PKP1a	DSC1	1-726	715-894	OA	(Smith & Fuchs, 1998)	1-726:715-894
DP	DSC1	1-176	715-894	OA	(Smith & Fuchs, 1998)	1-176:715-894
PKP1a	DP	1-168	1-584	Y2H	(Hatzfeld et al., 2000)	1-168:1-584
		1-286	1-584	Y2H, co-IP, Loc	(Kowalczyk et al., 1999)	
		1-726	1-1014	OA	(Smith & Fuchs, 1998)	
		1-726	1-2871	Loc	(Bornslaeger et al., 2001)	
PG	DP	1-745	1-2871	OA	(Smith & Fuchs, 1998)	1-745:1-584
The below data are on ODP isoforms that were not included in the main model.						
PKP3a	DSC1	1-18 & 51-797	715-894	Y2H, co-IP, Loc	(Bonné et al., 2003)	(1-18 + 51-797):715-894
PKP3a	DSG1	1-18 & 51-293	519-715 Or 715-1k	Y2H, co-IP	(Bonné et al., 2003)	(1-18 + 51-293):570-842
PKP3a	DP	19-50	1-2871	Loc	(Bonné et al., 2003)	(1-18 + 51-293):1-584 & 19-50:1-63
		1-18 & 51-293	1-584	Y2H, co-IP, Loc	(Bonné et al., 2003)	

		19-50	1-63	Y2H	(Bonné et al., 2003)	
PKP3a	DSC3	1-18 & 51-797	712-897	Y2H, co-IP	(Bonné et al., 2003)	(1-18 + 51-797):712-897
PKP3a	DSG3	1-18 & 51-797	641-999	Y2H, co-IP	(Bonné et al., 2003)	(1-18 + 51-797):641-999

Table S2A Binding Restraints The protein-protein binding restraints are shown along with the experimental data they are based on. Only residues that are modeled in our ODP model are included in the restraints. If multiple experiments provide data for a protein pair, the data from the experiment with the highest resolution is used. In columns 3, 4 (and 5), the green background (or text) represents the highest resolution information that was used to formulate the restraint, and gray represents other information that is at a lower resolution than the restraint. Experiment abbreviations are as follows: Y2H: Yeast 2 Hybrid, OA: Overlay Assay (in-vitro), Loc: Co-Localization assays, Co-IP: Co-Immunoprecipitation.

Protein Termini	Residues	Mean dist. (Å)	SE (Å)
DP-N	1-189	103	9.8
PG-N	1-106	229	4.5
PG-C	666-738	108	9
PKP1-N	1-285	158	11
PKP1-C	286-726	42	11
The below data are on ODP isoforms that were not included in the main model.			
PKP3-N	1-359	158	11
PKP3-C	360-797	42	11

Table S2B Immuno-EM Restraints The antibody-binding domains for the different termini, the mean distance of the termini from the plasma membrane, and the respective standard errors are shown (North et al., 1999). Domain names are per Fig. 1.

Protein Domain 1	Protein Domain 2	Experiment	Validation data	Reference
DP^{1-1014}	DP^{1-176}	OA	DP^{1-1014} binds to DP^{1-176}	(Smith & Fuchs, 1998)
$DSG1^{570-589}$	$DSC1^{715-734}$	Cryo-ET	Cadherin spacing: Distance between DSG1 membrane-bound region and DSC1 membrane-bound region is 7 nm	(Sikora et al., 2020)
$PG\text{-}N^{30-109}$	-	dSTORM	Distance of domain from membrane = 240 +/- 20 Å	(Stahley et al., 2016)

Table S3A Validation data not used in modeling The data not used in modeling is shown along with the corresponding references. Data for validation was obtained using the same reasoning as in Table S2A. Experiment abbreviations are as follows: OA: Overlay Assay, cryo-ET: cryo-electron tomography, dSTORM: direct stochastic optical reconstruction microscopy.

Protein Domain 1	Protein Domain 2	Experiment	Data	Reference
PG	DP	Y2H, co-IP	PG binds to DP	(Kowalczyk et al., 1997)
PG	$DSG1^{737-775}$	co-IP, Loc	Full PG binds to $DSG1^{737-775}$	(Troyanovsky, Troyanovsky, Eshkind, Krutovskikh, et al., 1994)
$PG^{123-632}$	DSG1	co-IP	$PG^{123-632}$ binds to DSG1	(Wahl et al., 1996)
PG	$DSG1^{663-958}$	ITC	Full PG binds to $DSG1^{663-958}$	(Choi et al., 2009)
PG	$DSC1^{857-894}$	co-IP, Loc	Full PG binds to $DSC1^{857-894}$	(Troyanovsky, Troyanovsky, Eshkind, Leube, et al., 1994)
$PG^{123-632}$	DSC1	co-IP	$PG^{123-632}$ binds to DSC1	(Wahl et al., 1996)
PG	$DSC1^{795-894}$	ITC	Full PG binds to $DSC1^{795-894}$	(Choi et al., 2009)
$DSG1^{571}$, $DSG1^{573}$	-	ABE	Residues are membrane-interacting	(Roberts et al., 2016)
$DP\text{-}N^{1-189}$	-	dSTORM	Distance of domain from membrane = 410 +/60 Å	(Stahley et al., 2016)

DP	DSC1$^{728-740}$	co-IP, Loc	Full DP binds to DSC1$^{728-740}$	(Troyanovsky, Troyanovsky, Eshkind, Leube, et al., 1994)
PG	DSC1$^{728-740}$	co-IP, Loc	Full PG binds to DSC1$^{728-740}$	(Troyanovsky, Troyanovsky, Eshkind, Leube, et al., 1994)

Table S3B Other data consistent with the data used in modeling Data from imaging and biochemistry experiments that is consistent with the data used for modeling is shown along with the corresponding references. Experiment abbreviations are as follows: dSTORM: direct stochastic optical reconstruction microscopy, cryo-ET: cryo-electron tomography, ABE: acyl biotin exchange assay., Y2H: Yeast-2-Hybrid, co-IP: Co-Immunoprecipitation, Loc: Co-Localization assays, ITC: Isothermal Calorimetry. Rows in gray represent data that is not consistent with the data used for modeling.

Protein 1	Residues in protein 1	Protein 2	Residues in protein 2
DP	1-20	DSC1	795-833
DP	21-60	DSC1	815-833
DP	21-40	DSC1	795-814
DP	61-100	DSC1	815-833
DP	141-177	DSC1	864-893
DP	178-237	PG	306-335
DP	238-267	PG	276-335
DP	61-80	PG	366-395
DP	81-100	PG	336-395
DP	101-140, 161-177	PG	306-395
DP	141-160	PG	306-425
DP	178-207	PG	246-305, 336-425
DP	208-237	PG	216-305, 336-395
DP	238-267	PG	216-275, 336-455
DP	268-297	PG	246-275
DP	328-357	PG	216-335
DP	448-507	PG	81-120, 126-275
DP	508-537	PG	61-100
DP	1-60	PKP1	141-180
DP	61-100	PKP1	141-160
DP	328-357	PKP1	1-20
DSC1	795-814	PG	636-658
DSC1	815-833	PG	336-605, 636-658
DSC1*	834-863	PG	276-575

DSC1*	864-894	PG	101-245
DSC1*	894	PG	101-155
DSC1	795-814	PG	661-673
DSC1	815-833	PG	606-635
DSG1	670-689	PG	606-673
DSG1	690-697	PG	456-673
DSG1*	698-727	PG	366-658
DSG1*	728-757	PG	101-275
DSG1*	758-765	PG	101-215
DSG1	766-785	PG	101-185
DSG1	786-805	PG	126-155
DSG1	670-689	PG	674-693
DSG1*	698-727	PG	659-660
DSG1	766-785	PG	186-215
DSC1	775-794	PKP1	201-220
DSC1	795-814	PKP1	181-220
DSC1	795-814	PKP1	161-180
DSC1	815-833	PKP1	161-220
DSG1	650-669	PKP1	181-220
DSG1	670-689	PKP1	161-220
DSG1	630-649	PKP1	201-220
DSG1	650-669	PKP1	221-240
DSG1	670-689	PKP1	141-160
DSG1	690-697	PKP1	181-200

Table S4 Protein-Protein contacts in the ODP All the contacts identified in at least 20% (yellow) to 25% (green) of the models in the ensemble are shown (Methods). Contacts consistent with sub-complexes of known structure are marked with an asterisk in column 1. See also Fig. 4 and Fig. S5.

Protein Domain	Residues	Mutation	Reference	Disease
PG-N	19	T → I	(Den Haan et al., 2009)	Naxos disease
PG-S	265	R → H	(Erken et al., 2011)	Naxos disease
PG-S	301	E → G	(Marino et al., 2017)	Naxos disease
PG-C	680-745	WEAAQSMIPI → GGCPEHDSHQ + Δ690-745	(McKoy et al., 2000)	Naxos disease
DP-S	287	N → K	(Whittock et al., 2002)	Skin Fragility - Woolly Hair Syndrome
DP-S	356	T → K	(Pigors et al., 2015)	Carvajal syndrome
DP-S	564	T → I	(Boulé et al., 2012; Keller et al., 2012)	Carvajal syndrome
DP-S	583	L → P	(Keller et al., 2012)	Carvajal syndrome
PKP1-S	502	R → H	COSMIC	Cancer Mutation
PG-N	4	M → V	COSMIC	Cancer Mutation
DSG1	788	E → K	COSMIC	Cancer Mutation
DSC1	841	Y → F	COSMIC	Cancer Mutation

Table S5 Mutations The mutations of interest in the different protein domains are shown along with the pathology associated with the mutations (Fig. 5, Results). Domain names are following Fig. 1.

Protein	Residue range	Number of beads or rigid bodies per protein copy	Number of degrees of freedom per protein copy (3 per flexible bead, 6 per rigid body)	Number of degrees of freedom across all copies of the protein
DP1	1-177	9 beads	27	108
	177-584	1 rigid body	6	24
PKP1a	1-243	13 beads	39	156
	244-700	1 rigid body	6	24
	701-726	2 beads	6	24
PG	1-125	7 beads	21	84
	126-673	1 rigid body	6	24
	674-745	4 beads	12	48
DSG1a	570-297	7 beads	21	42
	698-765	0* rigid body	0	0
	766-842	4 beads	12	24
DSC1a	715-833	6 beads	18	36
	834-894	0* rigid body	0	0
Total number of degrees of freedom				594

Immuno-EM and protein-protein binding restraints

Protein	Immuno-EM restraints per copy	Total number of immuno-EM restraints across all copies	Protein-protein binding restraints per copy	Total number of protein-protein binding restraints across all copies
DP1	1	4	3	12
PG	2	8	1	4
PKP1a	2	8	3	12
DSG1a	-	-	1	2
DSC1a	-	-	2	4
	Total immuno-EM restraints	20	**Total protein-protein binding restraints**	34

*DSG1a and DSC1a rigid bodies are counted as part of the complex with PG.

Table S6 Degrees of freedom The sampling degrees of freedom and the number of immuno-EM and protein-protein binding restraints associated with each protein are shown.

References

Al-Amoudi, A., Castaño-Diez, D., Devos, D. P., Russell, R. B., Johnson, G. T., & Frangakis, A. S. (2011). The three-dimensional molecular structure of the desmosomal plaque. *Proceedings of the National Academy of Sciences*, *108*(16), 6480–6485. https://doi.org/10.1073/pnas.1019469108

Alber, F., Dokudovskaya, S., Veenhoff, L. M., Zhang, W., Kipper, J., Devos, D., Suprapto, A., Karni-Schmidt, O., Williams, R., Chait, B. T., Rout, M. P., & Sali, A. (2007). Determining the architectures of macromolecular assemblies. *Nature*, *450*(7170), 683–694. https://doi.org/10.1038/nature06404

Bonné, S., Gilbert, B., Hatzfeld, M., Chen, X., Green, K. J., & Van Roy, F. (2003). Defining desmosomal plakophilin-3 interactions. *Journal of Cell Biology*, *161*(2), 403–416. https://doi.org/10.1083/jcb.200303036

Bonomi, M., Hanot, S., Greenberg, C. H., Sali, A., Nilges, M., Vendruscolo, M., & Pellarin, R. (2019). Bayesian Weighing of Electron Cryo-Microscopy Data for Integrative Structural Modeling. *Structure*, *27*(1), 175-188.e6. https://doi.org/10.1016/j.str.2018.09.011

Bornslaeger, E. A., Godsel, L. M., Corcoran, C. M., Park, J. K., Hatzfeld, M., Kowalczyk, A. P., & Green, K. J. (2001). Plakophilin 1 interferes with plakoglobin binding to desmoplakin, yet together with plakoglobin promotes clustering of desmosomal plaque complexes at cell-cell borders. *Journal of Cell Science*, *114*(4), 727–738. https://doi.org/10.1242/jcs.114.4.727

Boulé, S., Fressart, V., Laux, D., Mallet, A., Simon, F., De Groote, P., Bonnet, D., Klug, D., & Charron, P. (2012). Expanding the phenotype associated with a desmoplakin dominant mutation: Carvajal/Naxos syndrome associated with leukonychia and oligodontia. *International Journal of Cardiology*, *161*(1), 50–52. https://doi.org/10.1016/j.ijcard.2012.06.068

Buchan, D. W. A., & Jones, D. T. (2019). The PSIPRED Protein Analysis Workbench: 20 years on. *Nucleic Acids Research*, *47*(W1), W402–W407. https://doi.org/10.1093/nar/gkz297

Chodera, J. D. (2016). A Simple Method for Automated Equilibration Detection in Molecular Simulations. *Journal of Chemical Theory and Computation*, *12*(4), 1799–1805. https://doi.org/10.1021/acs.jctc.5b00784

Choi, H.-J., Gross, J. C., Pokutta, S., & Weis, W. I. (2009). Interactions of Plakoglobin and β-Catenin with Desmosomal Cadherins. *Journal of Biological Chemistry*, *284*(46), 31776–31788. https://doi.org/10.1074/jbc.M109.047928

Den Haan, A. D., Tan, B. Y., Zikusoka, M. N., Lladó, L. I., Jain, R., Daly, A., Tichnell, C., James, C., Amat-Alarcon, N., Abraham, T., Russell, S. D., Bluemke, D. A., Calkins, H., Dalal, D., & Judge, D. P. (2009). Comprehensive Desmosome Mutation Analysis in North Americans With Arrhythmogenic Right Ventricular Dysplasia/Cardiomyopathy. *Circulation: Cardiovascular Genetics*, *2*(5), 428–435. https://doi.org/10.1161/CIRCGENETICS.109.858217

Erken, H., Yariz, K. O., Duman, D., Kaya, C. T., Sayin, T., Heper, A. O., & Tekin, M. (2011). Cardiomyopathy with alopecia and palmoplantar keratoderma (CAPK) is caused by a *JUP* mutation. *British Journal of Dermatology*, *165*(4), 917–921. https://doi.org/10.1111/j.1365-2133.2011.10455.x

Garrod, D., & Chidgey, M. (2008). Desmosome structure, composition and function. *Biochimica et Biophysica Acta (BBA) - Biomembranes*, *1778*(3), 572–587. https://doi.org/10.1016/j.bbamem.2007.07.014

Goujon, M., McWilliam, H., Li, W., Valentin, F., Squizzato, S., Paern, J., & Lopez, R. (2010). A new bioinformatics analysis tools framework at EMBL-EBI. *Nucleic Acids Research*, *38*(Web Server), W695–W699. https://doi.org/10.1093/nar/gkq313

Hatzfeld, M., Haffner, C., Schulze, K., & Vinzens, U. (2000). The Function of Plakophilin 1 in Desmosome Assembly and Actin Filament Organization. *Journal of Cell Biology*, *149*(1), 209–222. https://doi.org/10.1083/jcb.149.1.209

Keller, D., Stepowski, D., Balmer, C., Simon, F., Guenthard, J., Bauer, F., Itin, P., David, N., Drouin-Garraud, V., & Fressart, V. (2012). De novo heterozygous desmoplakin mutations leading to Naxos-Carvajal disease. *Swiss Medical Weekly*. https://doi.org/10.4414/smw.2012.13670

Kohn, J. E., Millett, I. S., Jacob, J., Zagrovic, B., Dillon, T. M., Cingel, N., Dothager, R. S., Seifert, S., Thiyagarajan, P., Sosnick, T. R., Hasan, M. Z., Pande, V. S., Ruczinski, I., Doniach, S., & Plaxco, K. W. (2004). Random-coil behavior and the dimensions of chemically unfolded proteins.

Proceedings of the National Academy of Sciences, *101*(34), 12491–12496. https://doi.org/10.1073/pnas.0403643101

Kowalczyk, A. P., Bornslaeger, E. A., Borgwardt, J. E., Palka, H. L., Dhaliwal, A. S., Corcoran, C. M., Denning, M. F., & Green, K. J. (1997). The Amino-terminal Domain of Desmoplakin Binds to Plakoglobin and Clusters Desmosomal Cadherin–Plakoglobin Complexes. *Journal of Cell Biology*, *139*(3), 773–784. https://doi.org/10.1083/jcb.139.3.773

Kowalczyk, A. P., Hatzfeld, M., Bornslaeger, E. A., Kopp, D. S., Borgwardt, J. E., Corcoran, C. M., Settler, A., & Green, K. J. (1999). The Head Domain of Plakophilin-1 Binds to Desmoplakin and Enhances Its Recruitment to Desmosomes. *Journal of Biological Chemistry*, *274*(26), 18145–18148. https://doi.org/10.1074/jbc.274.26.18145

Marino, T. C., Maranda, B., Leblanc, J., Pratte, A., Barabas, M., Dupéré, A., & Lévesque, S. (2017). Novel founder mutation in French-Canadian families with Naxos disease: Letter to the Editor. *Clinical Genetics*, *92*(4), 451–453. https://doi.org/10.1111/cge.12971

McKoy, G., Protonotarios, N., Crosby, A., Tsatsopoulou, A., Anastasakis, A., Coonar, A., Norman, M., Baboonian, C., Jeffery, S., & McKenna, W. J. (2000). Identification of a deletion in plakoglobin in arrhythmogenic right ventricular cardiomyopathy with palmoplantar keratoderma and woolly hair (Naxos disease). *The Lancet*, *355*(9221), 2119–2124. https://doi.org/10.1016/S0140-6736(00)02379-5

Nilles, L. A., Parry, D. A. D., Powers, E. E., Angst, B. D., Wagner, R. M., & Green, K. J. (1991). Structural analysis and expression of human desmoglein: A cadherin-like component of the desmosome. *Journal of Cell Science*, *99*(4), 809–821. https://doi.org/10.1242/jcs.99.4.809

North, A. J., Bardsley, W. G., Hyam, J., Bornslaeger, E. A., Cordingley, H. C., Trinnaman, B., Hatzfeld, M., Green, K. J., Magee, A. I., & Garrod, D. R. (1999). Molecular map of the desmosomal plaque. *Journal of Cell Science*, *112*(23), 4325–4336. https://doi.org/10.1242/jcs.112.23.4325

Pigors, M., Schwieger-Briel, A., Cosgarea, R., Diaconeasa, A., Bruckner-Tuderman, L., Fleck, T., & Has, C. (2015). Desmoplakin Mutations with Palmoplantar Keratoderma, Woolly Hair and Cardiomyopathy. *Acta Dermato Venereologica*, *95*(3), 337–340. https://doi.org/10.2340/00015555-1974

Roberts, B. J., Svoboda, R. A., Overmiller, A. M., Lewis, J. D., Kowalczyk, A. P., Mahoney, M. G., Johnson, K. R., & Wahl, J. K. (2016). Palmitoylation of Desmoglein 2 Is a Regulator of Assembly Dynamics and Protein Turnover. *Journal of Biological Chemistry*, *291*(48), 24857–24865. https://doi.org/10.1074/jbc.M116.739458

Saltzberg, D. J., Viswanath, S., Echeverria, I., Chemmama, I. E., Webb, B., & Sali, A. (2021). Using Integrative Modeling Platform to compute, validate, and archive a model of a protein complex structure. *Protein Science*, *30*(1), 250–261. https://doi.org/10.1002/pro.3995

Sievers, F., Wilm, A., Dineen, D., Gibson, T. J., Karplus, K., Li, W., Lopez, R., McWilliam, H., Remmert, M., Söding, J., Thompson, J. D., & Higgins, D. G. (2011). Fast, scalable generation of high-quality protein multiple sequence alignments using Clustal Omega. *Molecular Systems Biology*, *7*(1), 539. https://doi.org/10.1038/msb.2011.75

Sikora, M., Ermel, U. H., Seybold, A., Kunz, M., Calloni, G., Reitz, J., Vabulas, R. M., Hummer, G., & Frangakis, A. S. (2020). Desmosome architecture derived from molecular dynamics simulations and cryo-electron tomography. *Proceedings of the National Academy of Sciences*, *117*(44), 27132–27140. https://doi.org/10.1073/pnas.2004563117

Smith, E. A., & Fuchs, E. (1998). Defining the Interactions Between Intermediate Filaments and Desmosomes. *Journal of Cell Biology*, *141*(5), 1229–1241. https://doi.org/10.1083/jcb.141.5.1229

Stahley, S. N., Bartle, E. I., Atkinson, C. E., Kowalczyk, A. P., & Mattheyses, A. L. (2016). Molecular organization of the desmosome as revealed by direct stochastic optical reconstruction microscopy. *Journal of Cell Science*, jcs.185785. https://doi.org/10.1242/jcs.185785

Teraoka, I. (2002). *Polymer solutions: An introduction to physical properties*. 2 John Wiley & Sons, Inc.

Troyanovsky, S. M., Troyanovsky, R. B., Eshkind, L. G., Krutovskikh, V. A., Leube, R. E., & Franke, W. W. (1994). Identification of the plakoglobin-binding domain in desmoglein and its role in plaque assembly and intermediate filament anchorage. *Journal of Cell Biology*, *127*(1), 151–160. https://doi.org/10.1083/jcb.127.1.151

Troyanovsky, S. M., Troyanovsky, R. B., Eshkind, L. G., Leube, R. E., & Franke, W. W. (1994). Identification of amino acid sequence motifs in desmocollin, a desmosomal glycoprotein, that are

required for plakoglobin binding and plaque formation. *Proceedings of the National Academy of Sciences*, *91*(23), 10790–10794. https://doi.org/10.1073/pnas.91.23.10790

Virtanen, P., Gommers, R., Oliphant, T. E., Haberland, M., Reddy, T., Cournapeau, D., Burovski, E., Peterson, P., Weckesser, W., Bright, J., Van Der Walt, S. J., Brett, M., Wilson, J., Millman, K. J., Mayorov, N., Nelson, A. R. J., Jones, E., Kern, R., Larson, E., … Vázquez-Baeza, Y. (2020). SciPy 1.0: Fundamental algorithms for scientific computing in Python. *Nature Methods*, *17*(3), 261–272. https://doi.org/10.1038/s41592-019-0686-2

Viswanath, S., Chemmama, I. E., Cimermancic, P., & Sali, A. (2017). Assessing Exhaustiveness of Stochastic Sampling for Integrative Modeling of Macromolecular Structures. *Biophysical Journal*, *113*(11), 2344–2353. https://doi.org/10.1016/j.bpj.2017.10.005

Wahl, J. K., Sacco, P. A., McGranahan-Sadler, T. M., Sauppe, L. M., Wheelock, M. J., & Johnson, K. R. (1996). Plakoglobin domains that define its association with the desmosomal cadherins and the classical cadherins: Identification of unique and shared domains. *Journal of Cell Science*, *109*(5), 1143–1154. https://doi.org/10.1242/jcs.109.5.1143

Whittock, N. V., Wan, H., Eady, R. A. J., Morley, S. M., Garzon, M. C., Kristal, L., Hyde, P., Irwin McLean, W. H., Pulkkinen, L., Uitto, J., Christiano, A. M., & McGrath, J. A. (2002). Compound Heterozygosity for Non-Sense and Mis-Sense Mutations in Desmoplakin Underlies Skin Fragility/Woolly Hair Syndrome. *Journal of Investigative Dermatology*, *118*(2), 232–238. https://doi.org/10.1046/j.0022-202x.2001.01664.x